Seafloor expression of oceanic detachment faulting reflects gradients in mid-ocean ridge magma supply

Samuel Howell, Jean-Arthur Olive, Garrett Ito, Mark Behn, Javier Escartin, Boris Kaus

Seafloor expression of oceanic detachment faulting reflects gradients in mid-ocean ridge magma supply

Samuel M. Howell[*1,2], Jean-Arthur Olive[3], Garrett Ito[2], Mark D. Behn[4,5], Javier Escartín[6], Boris Kaus[7]

*Corresponding author (**samuel.m.howell@jpl.nasa.gov**)

Affiliations

[1]*NASA Jet Propulsion Laboratory, California Institute of Technology, Pasadena, CA*

[2]*Department of Geology and Geophysics, University of Hawai'i at Mānoa, Honolulu, HI*

[3]*Laboratoire de Géologie, Ecole Normale Supérieure / CNRS UMR 8538, PSL Research University, Paris, France*

[4]*Department of Geology and Geophysics, Woods Hole Oceanographic Institution, Woods Hole, MA*

[5]*Department of Earth and Environmental Sciences, Boston College, Chestnut Hill, MA*

[6]*Marine Geosciences, Institut de Physique du Globe de Paris, CNRS UMR7154, Paris, France*

[7]*Institute of Geosciences, Johannes Gutenberg University Mainz, Mainz, Germany*

Abstract

Oceanic detachment faulting is a major mode of seafloor accretion at slow and ultraslow spreading mid-ocean ridges, and is associated with dramatic changes in seafloor morphology. Detachments form expansive dome structures with corrugated surfaces known as oceanic core complexes (OCCs), and often transition to multiple regularly-spaced normal faults that form abyssal hills parallel to the spreading axis. Previous studies have attributed these changes to along-axis gradients in lithospheric strength or magma supply. However, despite the recognition that magma supply can influence fault style and seafloor morphology, the mechanics controlling the transition from oceanic detachment faults to abyssal hill faults and the relationship to along-axis variations in magma supply remain poorly understood. This study investigates this issue using two complementary modeling approaches. The first consists of semi-analytical, two-dimensional (2-D) cross-axis models designed to address the fundamental mechanical controls on the longevity of normal faults. These 2-D model sections are juxtaposed in the along-axis direction to examine the response of the plan-view pattern of faults to along-axis variations in magmatic accretion in the absence of along-axis mechanical coupling. The second approach uses three-dimensional (3-D), time-dependent numerical models that simulate faulting and magma intrusion in a visco-elasto-plastic continuum. The primary variable studied through both approaches is the along-axis gradient in the fraction M of seafloor spreading that is accommodated by magmatism. The 2-D and 3-D results predict different abyssal hill spacing and orientation, however the plan-view geometry of self-emerging detachment faults predicted by the 3-D numerical models are well explained by the juxtaposed 2-D models. This indicates a first-order control by cross-axis effects of changing values of M. These models are also shown to explain the along-axis extent and plan-view curvature of the well-developed 13º20’N and Mt. Dent OCCs (Mid-Atlantic Ridge and Cayman Rise) in terms of quantifiable along-axis gradients in magma emplacement rates.

1. Introduction

The interplay between magmatism and faulting during seafloor spreading shapes the structure of mid-ocean ridges (MORs) and the abyssal hills that blanket ocean basins. Globally, seafloor created at decreasing spreading rates exhibits increasing fault size and rougher topography (e.g., Macdonald, 1982). This trend has been interpreted to reflect a change in the partitioning of magmatism and faulting during seafloor spreading, with slower-spreading segments exhibiting less plate separation accommodated through magmatic intrusion and more via normal faulting (e.g., Buck et al., 2005; Cannat et al., 2006; Olive et al., 2015).

Likewise, local changes in fault style and seafloor morphology along individual ridge segments (over along-axis distances of tens-of-kilometers) are also closely linked to changes in magma supply. For example, a detailed bathymetric analysis of the intermediate-spreading Chile Ridge revealed that abyssal hill-bounding faults become more prominent toward individual spreading segment ends, corresponding to inferred decreases in magmatic extension (Howell et al., 2016). These decreases roughly coincide with a reduction in the extent of partial melting as reflected in the chemistry of extruded basalts. Analogous along-axis variations in seafloor morphology are often even more pronounced at slow- and ultraslow-spreading MORs (e.g., Shaw 1992; Sempéré et al., 1993), where intra-segment variations in crustal thickness—a proxy for magma supply—are globally maximized (e.g., Cannat et al., 2003; Kuo and Forsyth, 1988; Thibaud et al., 1998).

One extreme change in seafloor morphology occurs along sections of slow and ultraslow spreading segments where abyssal hills associated with short-offset (up to 1-2 km) normal faults transition to the broad surfaces of oceanic core complexes (OCCs) that are formed by long-lived detachment faults (e.g., Tucholke et al., 1998; Cann et al., 1997). These detachments may be active for hundreds-of-thousands to millions of years, exposing tens-of-kilometers of lower crust and

64 mantle rocks along corrugated fault surfaces on the seafloor (**Figure 1a**). Oceanic detachment
65 faults are involved in the accretion of ~40% of new seafloor along the slow-spreading Mid-Atlantic
66 Ridge (Escartín et al., 2008; Cann et al., 2015). They also contribute to shaping large extents of
67 ultraslow-spread seafloor (e.g. Cannat et al., 2006; Dick et al., 2003). As such, they have been the
68 target of numerous studies in recent years.

69 Analytical models have employed force balance arguments to describe how the mechanical
70 properties of the brittle crust and upper mantle, or lithosphere, affect fault evolution and
71 abandonment, thereby controlling their lifespan and average spacing (Forsyth, 1992; Buck, 1993;
72 Lavier et al., 2000). Buck et al. (2005) combined analytical predictions with dynamic, two-
73 dimensional (2-D) continuum mechanics models to demonstrate that the size and spacing of
74 normal faults is directly controlled by the fraction of extension accommodated by the emplacement
75 of new magmatic material, *M*. The subsequent studies by Behn and Ito (2008) and Ito and Behn
76 (2008) confirmed the relationships between faulting styles and *M*, and quantified how *M* influences
77 the morphology of axial valleys and highs. Axial morphology was further addressed by Liu and
78 Buck (2018), who incorporated feedbacks between axial relief, magma pressure and dike injection
79 rate through scaling laws and 2-D numerical models.

80 Regarding faulting, the key premise of the above studies is that different values of *M* lead to
81 different opening rates at the magmatic center of the ridge axis (i.e., "neo-volcanic zone") relative
82 to the far-field spreading rate. This difference in opening rates controls how fast axis-bounding
83 normal faults migrate away from the neo-volcanic zone. When *M* is high (~1), faults migrate off-
84 axis rapidly and quickly enter areas of colder, stronger lithosphere where fault slip becomes
85 mechanically unfavorable. A new fault then forms on-axis, migrates off-axis, and the cycle repeats
86 to produce closely-spaced faults with minimal offset (**Figure 1a**).

As M decreases toward 0.5, faults migrate off-axis more slowly and stay active longer producing widely spaced faults that accumulate greater offsets. Where M=0.5, the rate of off-axis migration is zero and the fault can remain active indefinitely because it remains in an area of weak axial lithosphere (**Figure 1b**) (Buck et al., 2005; Tucholke et al., 2008). This theory is supported by observational evidence that long-lived detachment faults form in regions where magma supply is subdued (as suggested by positive gravity anomalies, e.g., Tucholke et al., 2008), albeit present (as indicated by the drilling of extensive gabbro units, e.g., Ildefonse et al., 2007).

Thus, extrapolating 2-D model behavior to natural ridge settings suggests that the along-axis location and extent of detachment faults should coincide with regions of M~0.5. In real systems, however, the 3-D coupling of stress and deformation likely perturb this ideal and simplified 2-D picture. Additionally, along-axis gradients in lithosphere strength may affect the development of "rider blocks" that cover detachment faults and thus impact their seafloor expression (Choi et al., 2013; Reston and Ranero, 2011; Smith et al., 2008).

Modeling of seafloor spreading and faulting at mid-ocean ridges in three dimensions has matured significantly in the last decade. Simulations of 3-D plate boundary evolution predict that dynamic instabilities associated with asymmetric accretion could spontaneously form transform faults and ridge-parallel detachment faults (Gerya, 2010), sensitive to the initial plate boundary geometry and rheological weakening assumptions (Gerya 2013). Püthe and Gerya (2014) captured spatial and temporal variations in magmatic and amagmatic accretion for slow and ultraslow ridges, and Liao and Gerya (2014) found that the generation of oceanic detachment faults in the late rifting-to-early spreading stage leads to asymmetric seafloor accretion. Differing from the above work, the study presented here focuses on the effects of along-axis variations in magma supply on the form and width of OCC's in a mature seafloor spreading environment.

Directly relevant to this study, the effects of along-axis gradients in magma supply were recently addressed in the 3-D numerical modeling study of Tian and Choi (2017). Their models predicted long-lived detachments that form near where M=0.5, but become unstable further along the ridge where M>0.5. However, these models were limited by their spatial resolution and did not clearly produce discrete abyssal hills.

In this study, we present the first 3-D models that simulate the transition between an OCC and well-resolved abyssal hill-scale faults due to along-axis variations in magmatically-accommodated spreading (dM/dy). We note that there are many other important factors that affect seafloor evolution in 3-D, including segmentation geometry and the associated variations in lithosphere thickness, as well as their temporal variability. In this study, however, we focus on the mechanical effects of the magmatic contribution to plate divergence. We begin by predicting the geometry of faulting along a ridge segment in map view by juxtaposing a series of individual 2-D (cross-axis) semi-analytical predictions (Buck et al. 2005; Behn and Ito 2008). These results serve as reference cases to compare with more realistic, fully 3-D numerical models that simulate along-axis mechanical coupling. Model predictions are then compared with two well-developed detachments exhibit a relatively simple tectonic structure, are located along linear ridge sections with no significant offsets, and have a relatively short geodynamic history (they are both active and rooting at the present-day rift valley).

2. Juxtaposed 2-D analytical models of fault evolution in map view

We build upon previous studies (Behn and Ito, 2008; Buck, 1993; Buck et al., 2005; Forsyth, 1992; Lavier et al., 2000; Olive and Behn, 2014; Shaw and Lin, 1996) to construct parametric, semi-analytical models of fault formation and evolution that are functions of M and time, t, in a 2-D section perpendicular to the ridge axis (See Appendix A for the full derivation). We modify

existing models to consider that detachment faults and associated abyssal hills occur predominantly on one side of the ridge axis for extended periods of time. We simulate the accretion of a seafloor area by juxtaposing numerous 2-D cross-sectional models, each with a different value of M ranging from 0.5-0.9. The monotonic variation in M can be interpreted as a linear variation in magma supply along a ridge axis, and in this way, the models predict the plan-view geometry of detachment faults and abyssal hills. We emphasize, however, that each cross-axis slice is truly 2-D because no information is shared between the adjacent slices.

The basic behavior of a single 2-D cross-section for a given value of M follows (see Appendix A for details). Shortly after a fault is formed, its brittle strength is reduced and the fault becomes the weakest part of the lithosphere. We assume that fault weakening occurs only through a reduction of cohesion (e.g., Lavier et al., 2000), and do not incorporate a reduction in the coefficient of internal friction. The pulling force needed to overcome the frictional resistance of the fault, F_F, is thus reduced. As the fault is pushed off-axis by magmatic spreading at the neovolcanic zone, it encounters thicker lithosphere, rotates to a lower dip, and accumulates finite displacement, which induces deformation of the adjacent footwall and hanging wall blocks. The first two effects increase F_F, while the last effect requires an additional pulling force to bend the surrounding lithosphere in response to slip on the fault plane, F_B. The sum of F_F and F_B describes the total pulling force needed to keep the fault slipping. Eventually, the required pulling force reaches the depth-integrated strength, F_I, of the un-faulted material at the ridge axis,

$$F_F + F_B \geq F_I. \quad (1)$$

This criterion (Eq. 1) is first met when the fault reaches the critical off-axis distance $x_c(M)$. At this point the fault is abandoned and a new fault breaks near the ridge axis, on the same side as the initial fault. The process repeats with the newly activated fault while the old, inactive one is

passively advected further off-axis.

We track the temporal evolution of two boundaries: (1) the position x_B of the footwall cutoff (FCO), or "breakaway," which is the very first part of the footwall that was exposed at the seafloor and is farthest from the ridge axis; and (2) the position x_T of the hanging wall cutoff (HCO), or "termination", which is where the footwall emerges from the seafloor closest to the ridge axis. The FCO (breakaway) lies on a rigid plate, and therefore migrates away from the ridge axis at the half spreading rate $u_{½}$. Its off-axis distance increases with time t according to:

$$x_B(t) = u_{½} t \,. \tag{2}$$

HCOs (terminations) migrate at a slower rate of $(2M - 1)$ when they are actively slipping ($x_T < x_c$), and at the half spreading rate when inactive. The location of a HCO (termination) is

$$x_T(M,t) = \begin{cases} (2M-1)\,u_{½}\,t & , \quad t < t_c \\ u_{½} t - 2x_c \left(\dfrac{1-M}{2M-1}\right) & , \quad t \geq t_c \end{cases} \tag{3}$$

where t_c is the time it takes for the FCO to migrate to the critical distance x_c, $t_c = x_c/((2M-1)u_{1/2})$.

The critical distance depends on M because M influences how quickly the active HCO migrates off axis (Eq. 3 for $t < t_c$) relative to the rate of slip on the fault, which in turn influences the pulling force required to sustain slip $F_F + F_B$ (see Appendix A). The critical distance also depends on lithosphere thickness, which is imposed to double over an off-axis distance of x=20 km and remain constant thereafter, simulating rapid hydrothermal cooling of the lithosphere, and slower, conductive, cooling beyond 20 km (e.g., Behn and Ito, 2008). For simplicity, in this study we assume that lithosphere thickness is uniform parallel to the ridge axis.

At time t=0, we consider the system to initiate with a single axially-continuous fault at the neo-

volcanic zone and the ridge axis ($x_B(y, t=0)=0$). As the system evolves, the initial FCO (breakaway) moves away from the ridge axis in a straight line parallel to the ridge axis at the half-spreading rate (**Figure 2a**). Where M=0.5, the active HCO does not move (x_T is fixed at zero from Eq. 3), marking the center of a long-lived detachment fault. For increasing values of M, the HCO migrates away from the ridge axis at a proportionally increasing rate, and so x_T increases linearly with M as predicted by Eq. (3) for $t<t_c$ (**Figure 2a**). The HCO first reaches x_c at the along-axis location where M is greatest, at which time the HCO becomes inactive and tectonic extension is instantaneously transferred to a new fault at x=0. From this point onward, the inactive HCO moves away from the ridge axis at the half-spreading rate (Eq. (3) for $t \geq t_c$).

With continued spreading, the location where the fault HCO reaches x_c migrates progressively towards the center of the detachment (the M=0.5 end of the model domain), producing an ever-narrowing detachment fault whose HCO is increasingly inclined to the ridge axis. The HCO traces out a characteristic curvature in plan-view (Eq. (3) for $t>t_c$), such that the along-axis width of the exposed detachment fault surface narrows toward the ridge axis (**Figure 2a**). An equation for the half-width of the active "toe" of the detachment (i.e., the along-axis distance between y=0 and the y-location where $x_T=x_c$) can be expressed as

$$w(t) = x_c \left(2u_{½} t \frac{M}{dy} \right)^{-1} . \quad (4)$$

This equation shows that w is an inverse function of time for a given along-axis gradient in M, hence explaining the narrowing of the detachment with time.

Figure 2b shows the predicted pattern of the cutoffs (active and inactive) for all faults that form over a given amount of time. To the side of the active detachment fault, numerous abyssal-hill forming normal faults form with a similar characteristic curve. The abyssal-hill faults become

198 more numerous and more closely spaced as *M* increases for the reasons predicted by Buck et al.
199 (2005) and Behn and Ito (2008). While the modeled abyssal hills are more closely spaced and
200 much more curved than natural ridge systems (e.g. **Figure 1**), the predictions of this first set of
201 models is useful for distinguishing the effects of along-axis variations in *M* in the absence of along-
202 axis stress and strain coupling from those produced by the full 3-D effects, which is illuminated
203 by the second modeling effort.

204 ## 3. 3-D Numerical Model

205 ### 3.1. Methods

206 We produce 3-D dynamic models using the computational code LaMEM (Kaus et al., 2016).
207 This code uses finite differences on a fully staggered mesh with the particle-in-cell method to solve
208 for conservation of mass and momentum in a visco-elastic-plastic continuum. A more complete
209 description of the numerical modeling method is presented in Appendix B. The Cartesian model
210 domain is 80 km in the spreading direction (*x*), *L*=20, 40, or 80 km in the along-axis direction (*y*),
211 and 40 km in the vertical direction (*z*). The domain is discretized uniformly with 256 × 64 × 128,
212 or 256 × 128 × 128 elements, respectively (**Figure 3**). We perform 24 simulations consisting of
213 ~2–8 million volume elements and ~150 million markers, run on 64–256 processors for ~10^3 time
214 steps in 24–350 hours (Table 1).

215 Our models include four primary material layers, listed here with increasing depth: (1) cold,
216 low-viscosity ocean, (2) cold, stiff, brittle lithosphere, (3) warmer, high-viscosity ductile material,
217 and (4) hot, low-viscosity asthenosphere. Layers (2)–(4) are controlled by an Arrhenius
218 dependence of viscosity on temperature (activation energy is 200 kJ/mol). The ocean layer
219 viscosity is 10^{-7} times that of the lithosphere to emulate a stress-free boundary condition. Extension
220 is imposed kinematically by pulling material out through the two sides at a half-spreading rate of

221 $u_{½}$=12.5 km/Myr, appropriate for many detachment-bearing slow-spreading mid-ocean ridges
222 (e.g., Tucholke et al., 2008).

223 The lithosphere deforms elastically until differential stress builds to the limit defined by the
224 Drucker-Prager brittle failure criterion, at which point deformation becomes plastic (see Appendix
225 B). This failure criterion generates planar volumes of localized shearing that represent fault zones.
226 The shear planes are further stabilized by reducing brittle strength with accumulated plastic strain
227 through a reduction of cohesion as in the juxtaposed 2-D models. At the same time, we allow the
228 plastic strain in the fault zone to heal so that fault strength (cohesion) recovers over a timescale of
229 20 kyr. These models contrast with prior models that additionally included an evolving coefficient
230 of friction in fault zones (Gerya, 2013; Püthe and Gerya, 2015; Liao and Gerya, 2015; Gülcher et
231 al., 2019).

232 We simulate magmatic accretion within a magma injection zone (MIZ) that defines the ridge
233 axis (x=0, y=0–L) (**Figure 3**). Within the MIZ, we impose a velocity divergence of $2\,u_{½}M(y)/\,w_{\mathrm{MIZ}}$
234 in a vertical column extending from the seafloor to the base of the axial lithosphere, with a width,
235 w_{MIZ}, of one element (Eq. B1). This produces a rate of horizontal MIZ widening of $2u_{½}M(y)$. As
236 the imposed divergence drives markers out of the dike elements, new markers are injected into the
237 MIZ to keep the marker density above a set value (^{3}4).

238 This scheme for magma injection ignores the fact that natural magma emplacement rates can
239 vary with depth. However, previous studies have shown that fault style is primarily sensitive to
240 the rate of injection within the brittle lithosphere and not below in the lower-stress regime of ductile
241 deformation (Olive et al., 2010). Further, when the depth-distribution of magma injection is
242 calculated from the evolving stress field surrounding the MIZ, the time-averaged magma injection
243 rates are relatively uniform throughout the lithosphere (Bialas et al., 2010). Our simplified

parameterization is thus adequate for the primary objectives of this study.

We consider north to be the direction y increases, and east to be the direction x increases. M increases linearly from 0.5 at the southern end (y=0) to maximum values of 0.6 to 0.9 at the northern end (y=L). The greatest modeled M exceeds the maximum value estimated at the Mid-Atlantic Ridge (Behn & Ito, 2008; MacLeod et al., 2009), ensuring that we capture the full plausible range.

We do not solve the heat equation in our model, rather we impose a temperature structure that controls viscosity and density in the lithosphere and upper-most asthenosphere. Temperature increases linearly from 0°C at the seafloor to 600°C at a depth H, which approximately defines the thickness of the brittle lithosphere. Along the ridge axis (y=0 to y=L), the lithosphere is imposed to have a uniform along-axis thickness of H_0=4 or 6 km (**Figure 3**), which is comparable to a low estimate of the seismogenic layer thickness at the axis of slow-spreading ridges (e.g. Parnell-Turner et al., 2016).

The depth to the 600°C isosurface is set to increase linearly with distance x away from the ridge axis to a maximum of H=2H_0 at x=20 km. For x>20 km, the base of the lithosphere remains flat at $2H_0$. Below the 600°C-isosurface, temperature increases linearly with depth to 1300°C at a depth of 1.5 H. This approximately defines the high-viscosity ductile layer. This temperature and resulting rheological structure is designed to simulate efficient hydrothermal cooling of the lithosphere to x=20 km off-axis, and less efficient conductive cooling beyond 20 km and below the brittle lithosphere. The thermal structure is uniform along the ridge axis, and is draped beneath each point of the model seafloor at each time step so as to preserve a time-invariant (i.e., steady-state) structure. In this way, we retain precise control over the geometry of the lithosphere and isolate the effect of along-axis changes in M on fault behavior (e.g., Behn and Ito, 2008).

3.2. 3-D Model Results and Comparison to 2-D Predictions

The 3-D numerical models exhibit faults that evolve through time, interact, and migrate away from and along the ridge axis (**Figure 4**). At the onset of extension, an axially continuous fault forms on one side of the ridge axis. After ~0.35 Myr, the hanging wall cutoff (HCO or termination) remains approximately fixed at y=0, and a long-lived detachment fault is established, centered at y=0 (M=0.5). Further north where M>0.5, models typically predict shorter-lived faults that migrate away from the axis ($t \geq 0.70$ in **Figure 4**). As these smaller faults develop, they may episodically link at depth with the stable detachment to temporarily form an axially-continuous slip plane (e.g., t=0.93 and 1.53 Myr in **Figure 4**), or they may briefly form on the opposite side of the axis (**Supplementary Movie S1**). Periodically, a new axially-continuous fault may form on the same or opposite side of the axis as the detachment, extinguishing the original detachment and adjacent smaller faults and creating a new detachment system, beginning the cycle over again (**Figure 5, bottom row**).

The seafloor in the footwall above the stable detachment fault eventually domes upwards away from the axis, and the initial HCOs curve in map view along the axis as they become inactive closer to the segment center at ever decreasing values of M. This behavior reflects a narrowing of the actively slipping plane of the detachment with time. At a given time, more gradual along-axis variations in M (i.e., smaller gradients, dM/dy) tend to produce wider detachments.

To understand the 3-D effects of dM/dy on fault evolution, including along-axis stress and strain, we compare the shapes of the HCOs with those of the juxtaposed 2-D models of Section 2 through time (**Figure 5**, and **Supplementary Movies S1-S3**). We find that the curved shape of the initial HCO bounding the detachment fault is very well described by the juxtaposed 2-D models. This result suggests that the shape of the detachment HCO is not heavily influenced by the 3-D

290 effects of along-axis mechanical coupling, and that the first order influence is the cross-axis effects
291 of different values of *M*.

292 The largest differences between the 3-D and juxtaposed 2-D predictions relate to abyssal hill
293 geometry away from the detachment (**Figure 2**, **Figure 5**). 3-D models predict abyssal hills to
294 form rapidly, with approximately axis-parallel trends, and for only one abyssal hill fault to be
295 active at a time. The abyssal hills are relatively straight and continuous, and their spacing is
296 relatively uniform. In contrast, the 2-D models predict that tectonism along the axis occurs on
297 multiple, highly inclined abyssal hill faults simultaneously (but still with only one active fault for
298 a given along-axis location). The more dramatic variability in the abyssal hill structures in the 2-
299 D models reflects the fact that that adjacent 2-D models do not interact. In the 3-D models, faults
300 initiate as planes along the ridge axis and their evolving form reflects some degree of mechanical
301 coupling in the along-axis direction. Still, the active slip planes of the 3-D faults and associated
302 HCOs display discontinuities or subtle jogs near the locations predicted by the 2-D models (**Figure**
303 **5, middle and right column**).

304 # 4. Discussion

305 ## 4.1. Comparison between models and seafloor observations

306 Our models provide a simple framework to quantitatively interpret seafloor morphology—in
307 particular the shape and along-axis extent of OCCs—in terms of along-axis variations in magma
308 supply alone. Our approach neglects effects related to the presence of transform faults, along-
309 segment variability in lithosphere thermal structure, composition and rheology, and other
310 geometrical and tectonic complexities (e.g., obliquity or non-linearity of the ridge axis, presence
311 of multiple synchronously active faults). The objective is to show that magma supply provides a
312 satisfactory, first-order explanation for the geometry of OCCs unaffected by ridge-transform

313 intersections.

314 We begin by comparing our model predictions with observations from the well-studied
315 13º20´N OCC on the Mid-Atlantic Ridge (**Figures 1, 6c**, **7**) (Escartín et al., 2017; MacLeod et al.,
316 2009; Searle et al., 2019; Smith et al., 2006; 2008). This OCC represents the footwall of a
317 detachment fault that has accumulated ~10 km of offset between its footwall cutoff (FCO,
318 breakaway) and the easternmost point of its HCO (termination), corresponding to <~0.8 Myr of
319 extension (Searle et al., 2019). The OCC FCO (breakaway) is a linear ridge that rises ~1 km above
320 surrounding seafloor (**Figure 7**) and exhibits significant backtilt (~30°) of the volcanic seafloor
321 due to rotation. Together, these observations are consistent with the hypothesis that the detachment
322 initiated as a continuous and linear fault spanning >20 km along-axis (Smith et al., 2008; Escartín
323 et al., 2017, Searle et al., 2019). It is noteworthy that while the OCC FCO does not strike parallel
324 to the ridge axis, its corrugations—which are reliable indicators of the direction of fault slip over
325 time—are clearly axis-perpendicular and spreading-parallel (Parnell-Turner et al., 2018). Escartín
326 et al. (2017) therefore inferred that the FCO initiated with its present-day NNW strike and migrated
327 westward as the detachment grew.

328 The resulting footwall dome has a topographic amplitude (~1 km) that is well captured by our
329 3-D simulations (**Figure 6**). The along-axis extent of the dome corresponds to ~50% of the length
330 of the FCO, which is consistent with the idea that the actively slipping portion of the detachment
331 narrowed over time, as predicted by both the juxtaposed 2-D and 3-D models. The sub-seafloor
332 portion of the detachment fault surface has recently been imaged through a high-resolution micro-
333 seismicity study (Parnell-Turner et al., 2017). The actively slipping surface, as illuminated by the
334 distribution of earthquakes, does not extend as far north and south as the FCO ridge, and exhibits
335 a mild curvature in map view (slightly concave to the west) like the HCO of the detachment

(**Figure 7a**). These characteristics are consistent with the behavior of the active slip surface in our 3-D model simulations (**Figure 6**).

In addition, more diffuse micro-seismicity is observed further north in the vicinity of two ~500-m high scarps striking N-NNE, and separated by ~4 km in the cross-axis direction. These features are interpreted as the scarps of abyssal-hill forming normal faults, and their relatively narrow separation and height is consistent with our model predictions in regions of higher *M*. In fact, *M* values of ~0.6 near the detachment, increasing to ~0.7 near the abyssal hill faults have been inferred through summation of observed fault heaves (MacLeod et al., 2009) (**Figure 7b**). Additionally, a large volcanic cone was emplaced at 13º26´N between these two scarps after their formation and subsequent flexural back-tilt (Escartín et al., 2017) (**Figure 1a, 7a**), consistent with increased magma supply to the nearby axis.

Our model thus provides a physically-constrained interpretation for the structure of the 13º20´N OCC and its connection with abyssal hills towards the north. This model is consistent with the interpretation of Searle et al. (2019), who find discontinuous magnetic patterns around the OCC that argue against the persistence of a single, segment-long detachment fault. In our interpretation, the detachment initiated as a ~20-km long normal fault whose HCO became inactive sooner in the north than in the south due to the greater melt supply, and subsequently migrated off-axis faster in the north. This prompted new, short-offset abyssal hill-bounding faults to form sequentially and act as the plate boundary in the north, while connecting with the active, on-axis detachment fault to the south whose surface expression narrowed through time. We note, however, that the complexities related to the initial obliquity of the detachment strike relative to the volcanic axis are not included in, nor predicted by, our modeling effort.

To further demonstrate the quantitative agreement between models and observations, we

359 compare the shape of the OCC using the equations arising from the juxtaposed 2-D models. While
360 the critical distance at which a new fault forms depends on M, we make the approximation here
361 that x_c is constant along-axis such that the solutions for the geometry of fault cutoffs (Eq. 2 and 3)
362 are fully analytical. This simplification is appropriate given the relatively small variation in x_c
363 predicted for M>0.6, i.e., over most of the model domain (**Figure 2**). The value of x_B is readily
364 obtained from a bathymetric map, as it represents the maximum offset on the detachment fault
365 (~10 km). By substituting Eq. (2) into (3) we can then recover the location of the position of the
366 HCO (termination), x_T, relative to the observed location of the FCO (breakaway), x_B. Inverting Eq.
367 (5) provides a way to estimate x_c from the observed spacing between abyssal hills (~4 km) and a
368 representative M value in the region where they form (0.7, consistent with the estimate of MacLeod
369 et al., 2009). This yields an average x_c of 1.5 km. The resulting detachment geometry, shown in
370 **Figure 7a**, envelopes the FCO ridge and OCC dome, and accurately predicts the narrowing of the
371 OCC toe over time. This result provides support that the scaling laws based on the cross-axis
372 influences of different values of M (Eq. 2, 3, and 5) adequately explain the plan-form stucture of
373 an OCC, and that the width of this OCC is plausibly controlled by an along-axis gradient in M
374 (Figure 8b), consistent with independent estimates (MacLeod et al., 2009).

375 **4.2. Inferring along-axis gradients in magma supply from detachment morphology**

376 To further test the validity of our proof-of-concept method for relating OCC geometry to
377 gradients in M, we apply it to an OCC where independent constraints on along-axis variability in
378 magma supply are available. The Mt. Dent OCC on the ultraslow-spreading Mid-Cayman
379 Spreading Center (**Figure 8**) (Hayman et al., 2011; ten Brink et al., 2002) exhibits a similar plan-
380 view shape to that of the 13°20′N OCC along the MAR, and is located in the middle of a linear
381 ridge section undergoing orthogonal spreading. Van Avendonk et al. (2017) recently conducted a

seismic experiment that provides insight into the thickness and nature of the oceanic crust along the axis of the Mid-Cayman Spreading Center (seismic profile along the dashed yellow line in **Figure 8**). Their seismic velocity model reveals that the crust—delineated by the 7 km/s P-wave velocity contour—is thinnest (< 4 km) on-axis near the Mt. Dent OCC, where it likely involves a large proportion of serpentinized peridotites (Harding et al., 2017). The seismic crust thickens considerably north and south of the OCC (**Figure 8c**), and the seismic velocity structure becomes more compatible with that of a basaltic crust 20–30 km away from the detachment where broad low-velocity zones are imaged at depths between ~3 and 7 km (Van Avendonk et al., 2017). Crustal thickness peaks have been documented near 18º05´N and at 18º32´N where vigorous basalt-hosted hydrothermal venting (i.e., the Beebe hydrothermal site: Connelly et al., 2012). These findings are consistent with Mt. Dent coinciding with a regional minimum in M at length scales of 10s of km, as was postulated for the 13º20´N OCC.

To extract quantitative constraints on dM/dy north and south of Mt. Dent, we again make use of Eqs (2), (3), and (5). The total offset on the OCC is estimated to be x_B=16 km. Determining x_c here is more challenging than north of the 13º20´N OCC because identifying abyssal hill bounding faults is not as straightforward. Elongated topographic features north and south of Mt. Dent have been interpreted as axial volcanic ridges (Van Avendonk et al., 2017), although a tectonic origin cannot be entirely ruled out. In either case, axial volcanic ridges or abyssal hill-bounding faults both act as a plate boundary to take up deformation in places where slip on the initial detachment fault has ceased. In the absence of strong constraints on x_c, we use the value inferred at 13º20´N (1.5 km) and estimate the value of dM/dy that best fits the shape of the Mt. Dent OCC (gray lines in **Figure 8a**). The corresponding $M(y)$ profile projected along the seismic profile of Van Avendonk (2017) is plotted in **Figure 8b**. It predicts an increase in M from 0.5 to ~0.7 between

405 Mt. Dent and the points of maximum crustal thickness north and south of the OCC.

406 Seismic tomography further reveals that the magma supply decreases beyond these points, as
407 one approaches the transform faults that bound the Mid-Cayman Spreading Center (Van Avendonk
408 et al. 2017). Our model thus only applies to the area shown in yellow in **Figure 8b,c** where magma
409 supply increases away from the OCC. Within this region, the relative increase in M inferred from
410 the OCC shape is ~40%, while seismic crustal thickness increases by ~200%. The suggestion of a
411 greater proportional increase in crustal thickness than M can stem from the fact that magma
412 emplacement rates vary drastically with depth, such that a single value of M averaged over the
413 whole brittle portion of the magma injection zone may not provide a reliable proxy for crustal
414 thickness. Olive et al. (2010) showed that OCC growth in numerical models can be achieved over
415 the full range of possible M values in the ductile asthenosphere (M_D) as long as magma is intruded
416 in the brittle lithosphere at a relative rate M_B~0.5. Our model thus only constrains M_B and dM_B/dy,
417 while crustal thickness reflects a combination of M_B and M_D. Additional information on the nature
418 of the crust is required to efficiently relate the plan-view shape of OCCs and crustal thickness. It
419 should also be noted that the very notion of seismic crustal thickness may not provide an accurate
420 proxy for magma supply in this ultraslow-spreading environment where the crust is likely
421 heterogeneous and complex (e.g., Harding et al., 2017).

422 **4.3. Limitations of the 3-D numerical model and potential future directions**

423 There are several potential areas of improvement in our modeling approach that would allow
424 more realistic 3-D simulation of the natural behavior of mid-ocean ridge spreading segments.

425 First, to control lithosphere structure both along and across axis, we formally ignore the thermal
426 evolution of the lithosphere. Solving conservation of energy in future studies and allowing magma

injection to affect the thermal structure (e.g., Behn & Ito, 2008) will provide a better understanding of how natural lithosphere structures control fault morphology and development.

Second, we have simplified magma injection processes by assuming that injection rates are uniform with depth within the lithosphere and prescribed a priori along the ridge axis. Because injection rates can vary as a function of the local stress field and magma supply (e.g., Behn et al., 2006; Qin and Buck, 2008), the details of brittle deformation and the surface expression of faulting would be better captured by allowing dike opening rate (e.g., Bialas et al., 2010) as well the level that dikes rise in the crust (Liu and Buck 2018) to respond to the local stress field. The next generation of mid-ocean ridge models should focus on incorporating self-consistent melting and accretion processes in order to enable more quantitative comparisons between simulated crustal structure (e.g., faulting and crustal thickness) with seafloor observations.

Third, we simplify spontaneous brittle faulting by reducing only cohesion with increasing strain and assuming a constant fracture healing rate. Recently, Gülcher et al. (2019) demonstrated that the development of individual OCCs is strongly controlled by fracture healing rates, and their numerical results deviate significantly from the classic "rolling hinge" model of detachment faulting. Thus, there is a need for future studies that identify the most appropriate numerical approaches to fault strength evolution.

5. Conclusions and Perspectives

Both the juxtaposed 2-D models and 3-D dynamic models predict that a linear gradient in magmatically accommodated extension along a slow-spreading mid-ocean ridge can induce a transition from long-lived detachment faults to short-lived normal faults. Consistent with previous 2-D studies, long-lived detachment faults are predicted to be centered where the magmatic fraction of seafloor spreading, M, is ~0.5. In juxtaposed 2-D models as well as the full 3-D models, the

450 exposed footwall surface of a mature detachment is bound by a curved hanging wall cutoff
451 (termination) such that the detachment surface is narrowest near the ridge axis, and widens with
452 distance (or age) away from the axis.

453 Abyssal hill-forming normal faults are predicted to form adjacent to the detachment fault where
454 M>0.5. The 2-D models predict many active, highly inclined faults that are inconsistent with
455 geological observations, while the 3-D models predict only one active, relatively straight abyssal-
456 hill fault at a time. While the cross-axis effects of varying M are of first-order importance in
457 controlling the large-scale structure of OCCs, the along-axis stress and strain coupling is more
458 important to the detailed structure of the adjacent abyssal hill faults. The 3-D models produce
459 prominent features that resemble those of natural systems, including detachment faults with
460 upward doming surfaces, a widening of the detachment surface with distance away from the ridge
461 axis (as bounded by curved inactive HCO), and multiple abyssal hill-forming faults adjacent to the
462 detachment that approximately parallel the ridge axis.

463 Smith et al. (2008) describe two possible scenarios for the periodic formation of oceanic core
464 complexes and abyssal hills in their study of the Mid-Atlantic Ridge (MAR) in the 13º N area: a
465 "continuous fault" model and a "consecutive fault" model. In their continuous fault model, a single
466 detachment can span large lengths of individual ridge segments (like that from ~12º50' N to
467 ~13º40' N). Crust of the median valley floor may be transferred from the hanging wall to the
468 footwall along faults that root onto the master detachment at depth, creating abyssal hills between
469 exposed detachment surfaces. This is akin to the "rider block" model (Choi et al., 2013; Reston
470 and Ranero, 2011), in which the transfer of material onto the footwall (and thus the formation of
471 abyssal hills vs OCCs) is promoted by greater resistance to continued slip between the footwall
472 and the rider block material. This implies that M can be ~0.5 over large distances (like the MAR

473 near 13°N), but that there may be shorter wavelength variations in the mechanical favorability for
474 continued slip. Such variability could manifest as a change in the coefficient of friction on the
475 detachment surface (e.g., due to variations in lithology and/or alteration) and/or the dip of the
476 detachment fault beneath the rider block crust.

477 Alternatively, the consecutive fault model considers detachment fault surfaces that are
478 discontinuous along the ridge axis. Smaller normal faults that form abyssal hills do not necessarily
479 root at the master detachments, thus requiring an along-axis transition from long-lived detachment
480 faulting to periodic normal faulting—here attributed to variations in *M*. The consecutive fault
481 model is consistent with variations in *M* over length scales that are shorter than individual
482 segments. Along-axis variations in magma supply shorter than the segment scale are well
483 documented (e.g., Kuo and Forsyth, 1988). When these sub-segment-scale variations occur in
484 magmatically robust ridge sections with *M* well above 0.5 everywhere (e.g., OH1 segment along
485 the MAR, Hooft et al., 2000; Dunn et al., 2005), detachments cannot form and variations in the
486 seafloor expression of magma supply gradients are subdued (e.g., Howell et al., 2016). By contrast,
487 at segments with an overall magma supply close to *M*=0.5, small gradients are likely to produce
488 along-axis transitions in the mode of accretion (detachment vs. abyssal-hill forming faults), as
489 shown in our models. Indeed, the study by Searle et al. (2019) shows discontinuous magnetic
490 patterns at the 13°N OCC that seem inconsistent with a single, segment-long detachment fault,
491 instead supporting the independent evolution of OCCs and detachments.

492 Identifying which OCC-bearing ridge segments are better explained by continuous faulting
493 (rider blocks) and which are better explained by consecutive faulting (narrowing detachments as
494 predicted here) may require further analysis of existing seismic data or the collection of new data.
495 Subsequent analyses must delineate the geometry of internal fault surfaces and distinguish fault

surfaces from other sources of crustal heterogeneity. For example, inter-crustal seismic reflections imaged in an area of seafloor containing an OCC-like structure between the Mid-Atlantic Ridge and the Canary Islands were interpreted as an OCC fault zone underlying abyssal-hill forming rider blocks (Reston and Ranero 2011). More such studies on other (younger) OCCs are needed. Further, new analyses of seismic data should estimate the degree to which crustal thickness varies along-axis to test for corresponding variations in *M*.

Table 1. Summary of 3-D models run. Columns are respectively lithosphere thickness, axis length, minimum and maximum magma supply, magma supply gradient, and mean magma supply.

H_0 [km]	L [km]	Ms	Mn	$\Delta M/\Delta y$	$\lvert M \rvert$
4, 6	20	0.5	0.6	0.0050	0.55
		0.5	0.7	0.0100	0.60
		0.5	0.8	0.0150	0.65
		0.5	0.9	0.0200	0.70
	40	0.5	0.6	0.0025	0.55
		0.5	0.7	0.0050	0.60
		0.5	0.8	0.0075	0.65
		0.5	0.9	0.0100	0.70
	80	0.5	0.6	0.0013	0.55
		0.5	0.7	0.0025	0.60
		0.5	0.8	0.0038	0.65
		0.5	0.9	0.0050	0.70

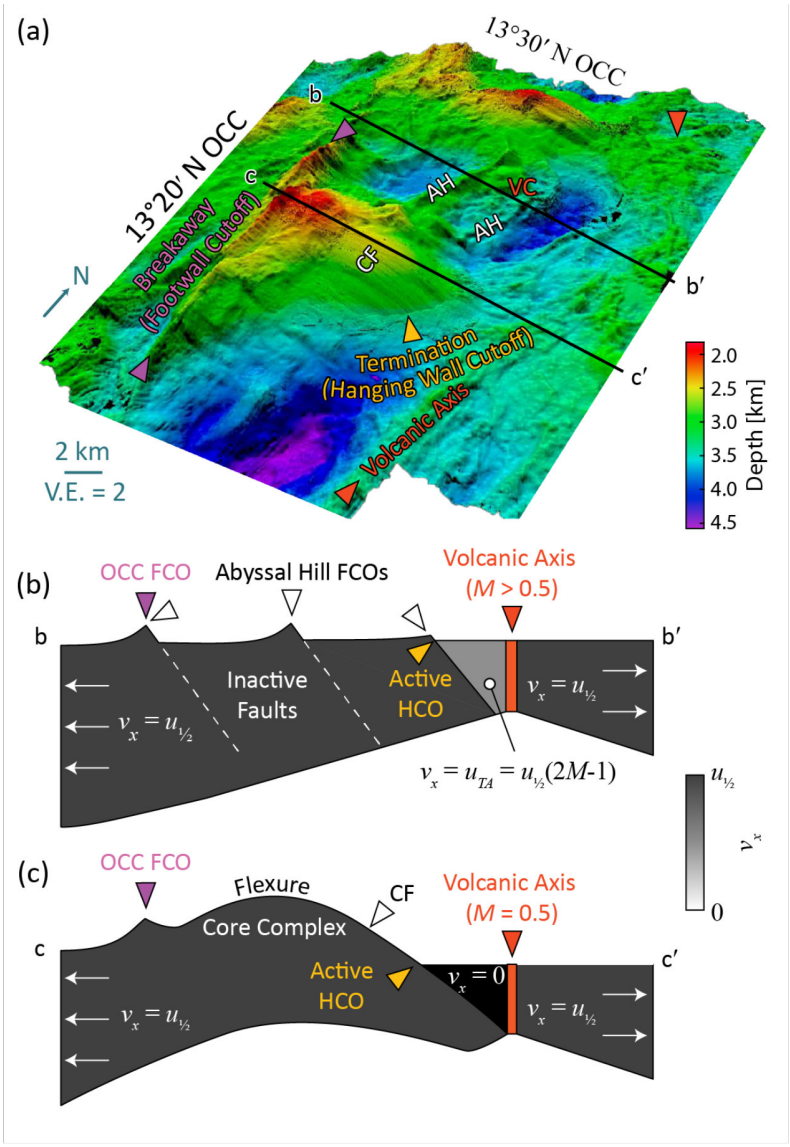

517 **Figure 1.** (a) 3-D perspective view of the bathymetry of the Mid-Atlantic Ridge axis around the
518 13°20¢Nand 13°30¢Noceanic detachments showing the different structural elements associated
519 with oceanic core complexes (OCC's). CF marks the corrugated OCC surface, AH marks the
520 abyssal hill normal faults, and VC marks an off-axis volcanic cone. Vertical exaggeration is 2. The
521 map includes both shipboard and AUV high-resolution bathymetry, acquired during the ODEMAR
522 2013 cruise (doi:10.17600/13030070) (Escartín et al., 2017). (b) 2-D schematic of an axis-
523 perpendicular cross-section along line b-b′ in (a), showing magmatic injection at the ridge axis

(orange), and tectonic spreading accommodated by the development and abandonment of short-throw, high-angle normal faults that form abyssal hills to the west of the ridge axis. (c) Cross-section beneath line c-c′ in (a), showing a single detachment fault that forms the OCC on the west side of the axis.

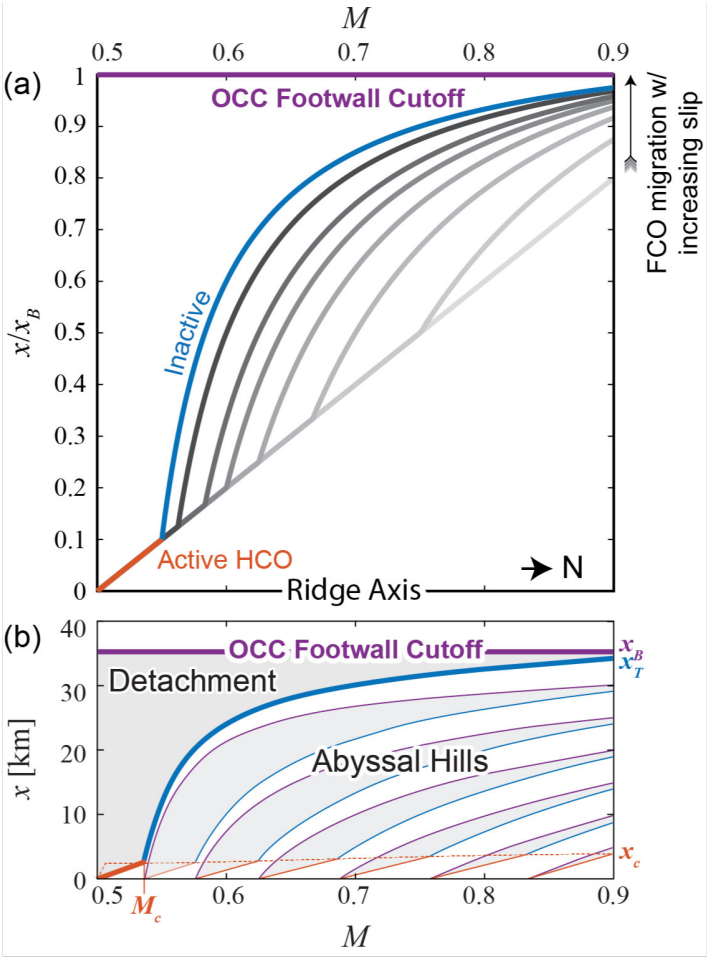

529 **Figure 2.** Example of juxtaposed 2-D semi-analytical solutions of fault geometry in map view
530 with x being the spreading direction and M varying linearly with distance along a ridge axis (axial
531 lithosphere thickness is H_0=4km, and lithosphere thickness H increase to 8 km at a distance of
532 x=20 km). (a) Evolution of the inactive HCO (termination) of a single detachment fault with the
533 vertical axis normalized by the off-axis FCO (breakaway) distance, x_B. Grey curves indicate the
534 HCO trace for different timesteps with darker colors indicating greater time. (b) Curves show
535 actively slipping HCOs (orange) and inactive HCOs (blue) when the FCO (purple) is located at a
536 distance ~10 times the critical distance after which the detachment HCO becomes inactive x_c
537 (orange dashed line). Shaded grey regions represent exposed fault scarps. Note that x_c shows
538 minimal variation over the range in M for the models studied here (for M>0.5).

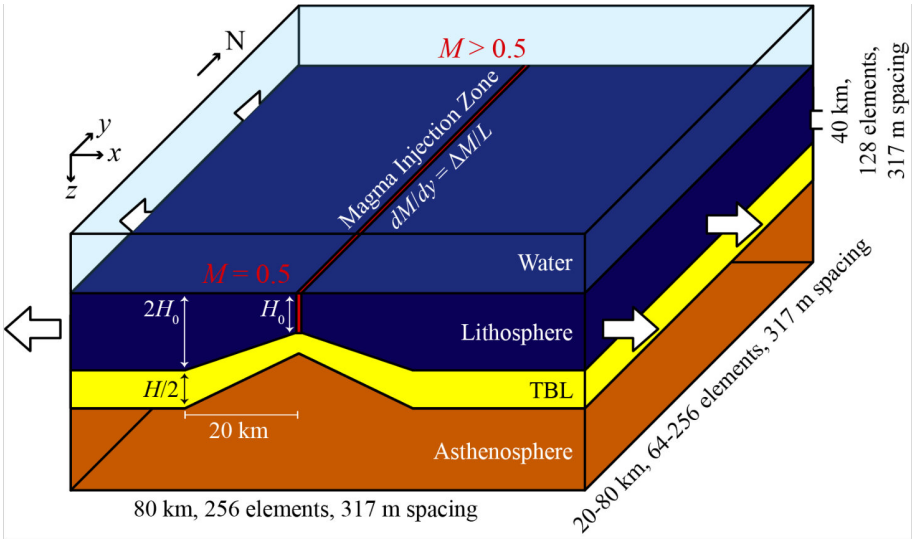

Figure 3. 3-D numerical model setup: a low-viscosity "ocean" (transparent blue) overlays a visco-elasto-plastic lithosphere (solid blue) defined by temperature that increase from 0° at the surface to 600 °C at a depth of H. The lithosphere transitions to a 1300 °C viscous asthenosphere (orange) across a thermal boundary layer (TBL, yellow) between depths of H and 1.5 H. The depth H of the 600 °C isosurface doubles from H_0 at the ridge axis to $2H_0$ at a distance 20 km from the axis. Material is injected in a narrow "Magma Injection Zone" (MIZ) that defines the ridge axis (red). The rate of injection imposes the fraction of total extension accommodated magmatically, M. The left and right model boundaries have zero shear traction and a Dirichlet normal velocity condition equal to half spreading rate, $\pm u_{1/2}$. The front and back boundaries have zero normal velocities and zero shear tractions. The bottom allows for free material in and out flow, the top has imposed inflow that conservatives water volume, and both boundaries have zero shear tractions.

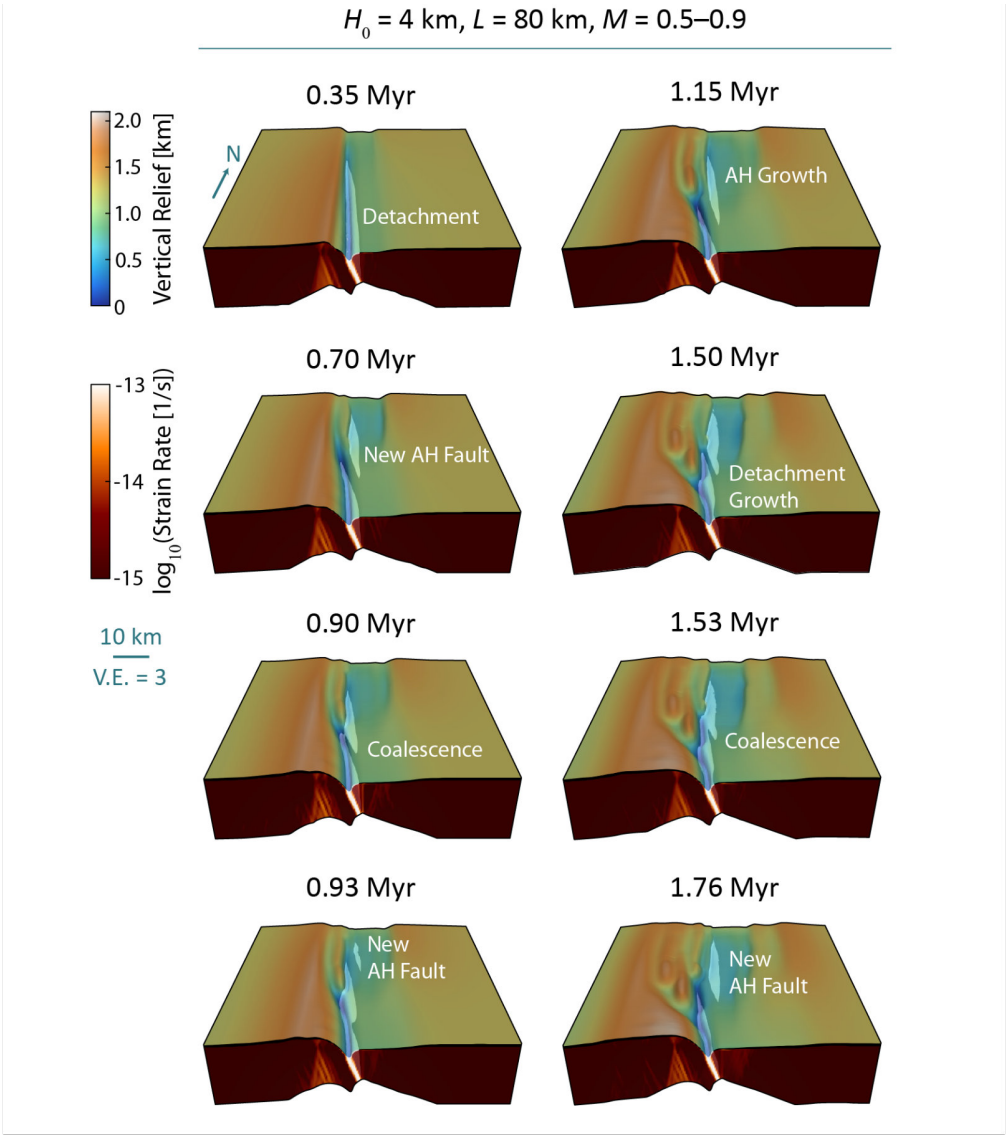

551 **Figure 4.** The evolution of a 3-D simulation (H_0=4 km, L=80 km, M=0.5–0.9). A stable
552 detachment fault is center on the south end of the model where M=0.5, while periodic normal
553 faulting produces abyssal hills (AH) further north where M>0.6. The simulation begins with a
554 cycle of abyssal hill formation and growth (0.70 Myr), until eventually the actively slipping plane
555 of the abyssal hill fault coalesces with that of the long-lived detachment, forming a single
556 continuous fault at depth (0.93 Myr). The cycle then repeats with the formation of a new abyssal
557 hill, while the detachment fault remains fixed at the axis. A second episode of fault coalescence
558 occurs at 1.53 Myr. Vertical exaggeration (V.E.) is 3:1.

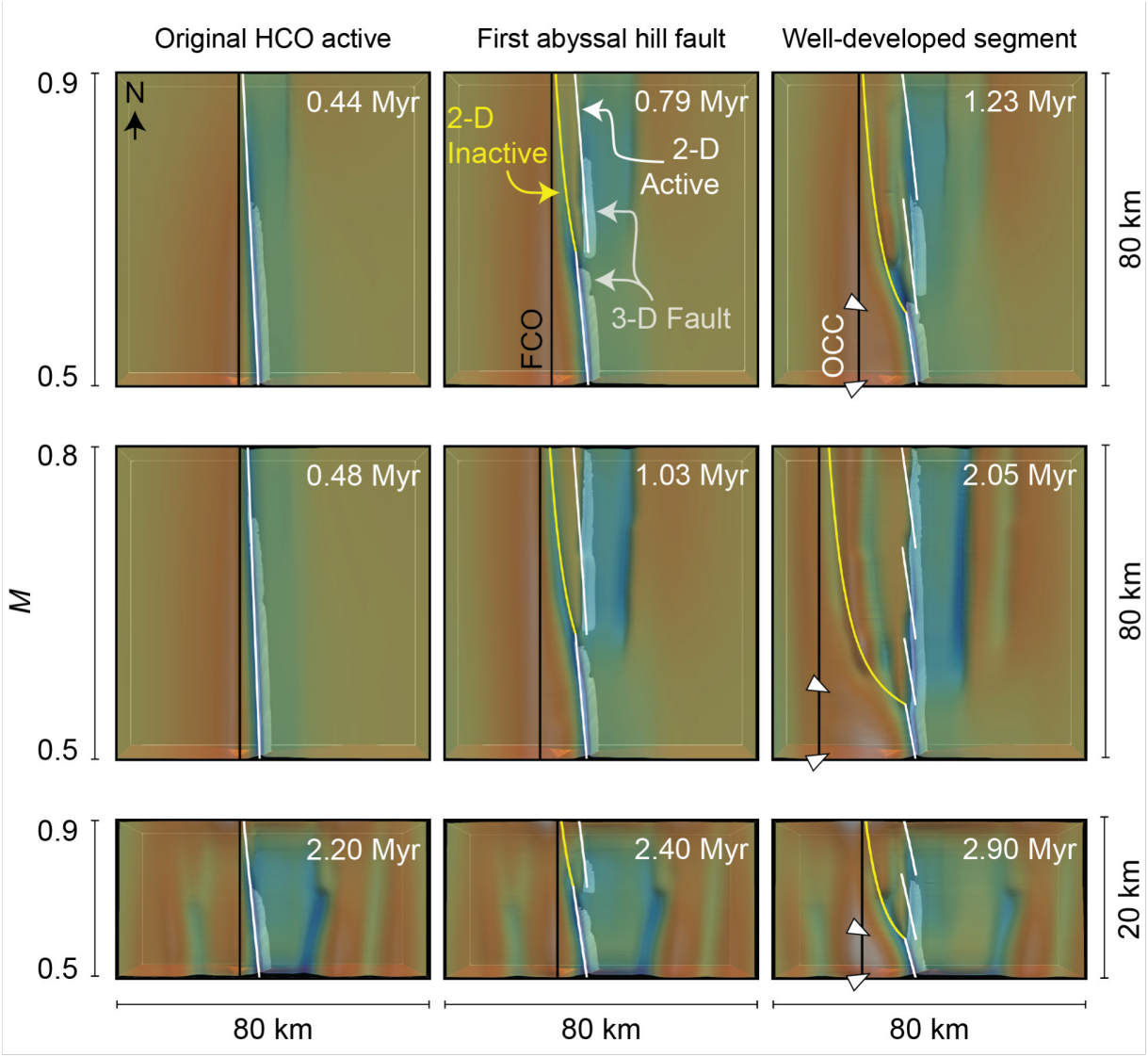

559 **Figure 5.** Rows show shaded bathymetric maps (colored as in **Figure 4**) of model seafloor for
560 three separate numerical simulations with H_0=4 km, L=80, M=0.5–0.9 (top), H_0=4 km, L=80,
561 M=0.5–0.8 (middle), and H_0=4 km, L=20, M=0.5–0.9 (bottom). The model surface is translucent
562 to reveal an internal isosurface of the actively slipping fault zone (where cohesion is zero).
563 Columns show the time step immediately before the first abyssal hill forms separately from an
564 axially-continuous detachment (left), shortly after the first abyssal hill forms (middle), and after
565 the second abyssal hill forms (right). The lowermost row shows an active OCC on the west side
566 of the ridge axis, with older OCCs visible on either side of the axis. Superimposed on the maps are

567 predictions of the 2-D models of the initial detachment FCO (black line), active fault HCOs (white
568 line), and the inactive detachment HCO (yellow line). Note the similarity in the along-axis extent
569 and approximate jogs of the 3-D model's active HCOs with the segmented HCOs predicted by the
570 juxtaposed 2-D models. The shape of the inactive detachment HCO is especially well explained
571 by the 2-D solutions (yellow).
572

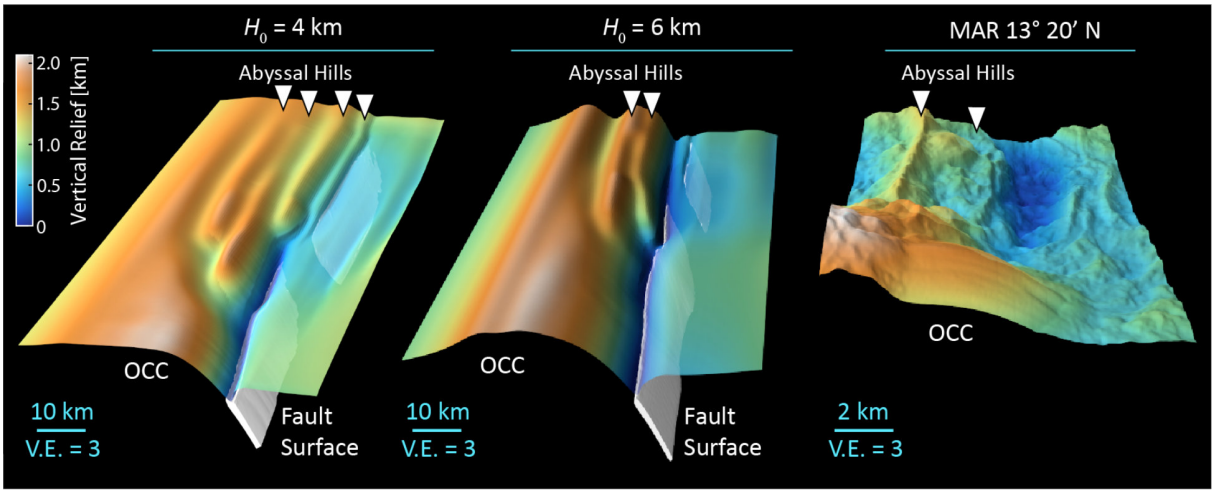

573 **Figure 6.** 3-D perspective views of oceanic detachment faults (south end) transitioning to abyssal
574 hill normal faults (north end, white triangles) for models with L=80 km, M=0.5–0.9, for H_0=4 km
575 (left) and 6 km (center), and of the Mid-Atlantic Ridge segment 13° 20'N (right). The active model
576 detachment surface (white isosurface, total cohesion loss) is separate from the newly formed
577 normal fault surface beneath the abyssal hills at the time step shown. The curvature of the
578 detachment fault HCO is greater in the model with thinner, weaker lithosphere (H_0=4 km). Vertical
579 exaggeration (V.E) is 3:1.

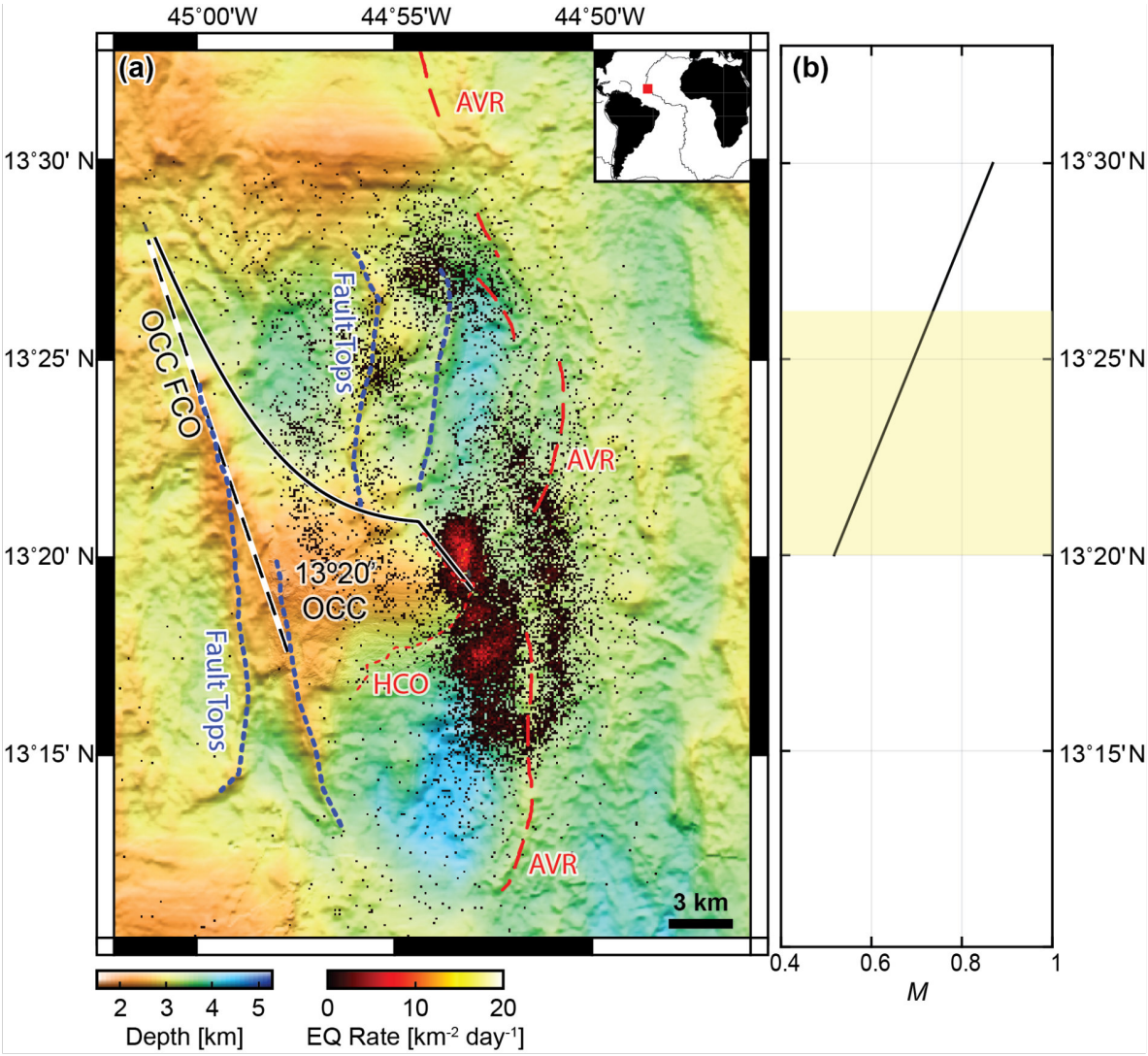

580

581 **Figure 7**. (a) Bathymetric map of the 13º20´N OCC on the Mid-Atlantic Ridge, showing a cloud
582 of microseismicity recorded over a 6-month period in 2014 (modified from Parnell-Turner et al.,
583 2017). Focal mechanisms show that the western cloud of seismicity (with elevated earthquake
584 rates) is mainly compressional, while the deeper, easternmost band of seismicity consists mainly
585 of normal faulting events on the detachment fault. Thick red dashed line marks the axial volcanic
586 ridge (AVR, as mapped by McLeod et al., 2009) and corresponding neo-volcanic axis. The thin
587 red dashed line indicates detachment termination (hanging wall cutoff) as mapped by Escartín et
588 al. (2017) and Searle et al. (2019). Dashed blue curves show the top of major faults, including the

589 detachment breakaway (footwall cutoff). The solid black curve marks the inferred location of the
590 inactive and active termination using Eqs. (2), (3), and (5) assuming x_B=10 km, x_c=1.5 km, and the
591 *M* distribution shown in panel (b) projected along the North-South direction. The corresponding
592 model breakaway is shown as the black-and-white dashed line. (b) *M* distribution vs. latitude, used
593 to visually fit (with the black curve) the inferred geometry of the 13º20´N OCC breakaway and
594 termination. The model variation in *M* is roughly consistent with the independent estimate of
595 MacLeod et al. (2009), who predicted *M*~0.6 – 0.7 between ~13º21' and ~13º25'N. The yellow
596 area marks the along-axis window within which *M* likely increases away from the detachment, and
597 where our scaling laws thus apply. This is because the 13º30'N OCC to the North is likely
598 associated with a local decrease in magma supply not accounted for in the model shown in panel
599 b.

600

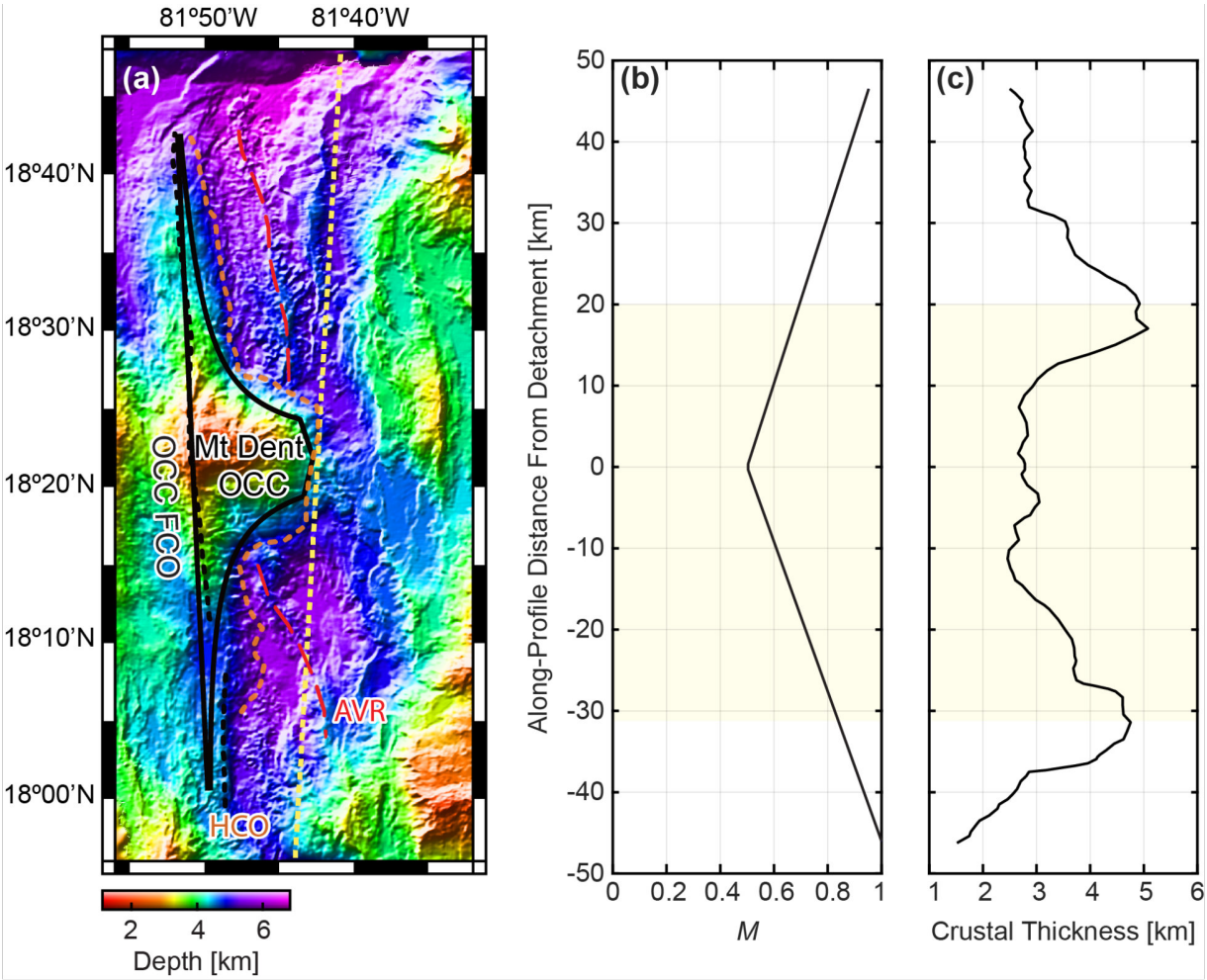

601

602 **Figure 8.** (a) Bathymetric map of the Mount Dent OCC on the Mid-Cayman Spreading Center
603 (Connelly et al. 2012). Black lines correspond to predictions of Eqs. (2) and (3) that visually
604 capture the overall shape of the Mt. Dent termination and breakaway, assuming x_B=16 km and
605 x_c=1.5 km. The termination (hanging wall cutoff) as interpreted by Van Avendonk et al. (2017) is
606 shown as a pink dashed line, along with the axial volcanic ridge (AVR, red dashed curve), inferred
607 by the same authors. The black dashed curve marks the crest of the breakaway ridge (footwall
608 cutoff). (b) *M* distribution used to produce the model OCC shape mapped in panel (a). (c) Crustal
609 thickness along the dashed yellow line plotted in panel (a) inferred from the depth of the 7 km/s
610 P-wave velocity contour from Van Avendonk et al. (2017). The yellow area marks the along-axis

window within which *M* likely increases away from the detachment, and where our scaling laws thus apply. Seismic tomography suggests that the magma supply decreases beyond this region as one approaches the transform faults that bound the Mid-Cayman Spreading Center to the North (~18º50'N) and South (~17º50'N) (Van Avendonk et al., 2017).

615 **References**

616 Balay, S., Abhyankar, S., Adams, M., Brown, J., Brune, P., Buschelman, K., Dalcin, L.D.,
617 Eijkhout, V., Gropp, W., Kaushik, D., 2017. PETSc Users Manual Revision 3.8. Argonne
618 National Lab.(ANL), Argonne, IL (United States).

619 Balay, S., Gropp, W.D., McInnes, L.C., Smith, B.F., 1997. Efficient management of parallelism
620 in object-oriented numerical software libraries, in: Modern Software Tools for Scientific
621 Computing. Springer, pp. 163–202.

622 Behn, M.D., Ito, G., 2008. Magmatic and tectonic extension at mid-ocean ridges: 1. Controls on
623 fault characteristics. Geochem. Geophys. Geosystems 9.

624 Bialas, R.W., Buck, W.R., Qin, R., 2010. How much magma is required to rift a continent? Earth
625 Planet. Sci. Lett. 292, 68–78. https://doi.org/10.1016/j.epsl.2010.01.021

626 Buck, W.R., 1993. Effect of lithospheric thickness on the formation of high-and low-angle normal
627 faults. Geology 21, 933–936.

628 Buck, W.R., Lavier, L.L., Poliakov, A.N.B., 2005. Modes of faulting at mid-ocean ridges. Nature
629 434, 719–723.

630 Cai, M., Nonaka, A., Bell, J.B., Griffith, B.E., Donev, A., 2014. Efficient variable-coefficient
631 finite-volume Stokes solvers. Commun. Comput. Phys. 16, 1263–1297.

632 Cann, J.R., Blackman, D.K., Smith, D.K., McAllister, E., Janssen, B., Mello, S., Avgerinos, E.,
633 Pascoe, A.R., Escartin, J., 1997. Corrugated slip surfaces formed at ridge–transform
634 intersections on the Mid-Atlantic Ridge. Nature 385, 329.

635 Cann, J.R., Smith, D.K., Escartín, J., Schouten, H., 2015. Tectonic evolution of 200 km of Mid-
636 Atlantic Ridge over 10 million years: Interplay of volcanism and faulting. Geochem.
637 Geophys. Geosystems 16, 2303–2321.

638 Cannat, M., Rommevaux-Jestin, C., Fujimoto, H., 2003. Melt supply variations to a magma-poor
639 ultra-slow spreading ridge (Southwest Indian Ridge 61° to 69°E). Geochem. Geophys.
640 Geosystems 4, n/a-n/a. doi:10.1029/2002GC000480
641 Cannat, M., Sauter, D., Mendel, V., Ruellan, E., Okino, K., Escartín, J., Combier, V., Baala, M.,
642 2006. Modes of seafloor generation at a melt-poor ultraslow-spreading ridge. Geology 34,
643 605–608.
644 Choi, E., Buck, W.R., Lavier, L.L., Petersen, K.D., 2013. Using core complex geometry to
645 constrain fault strength. Geophys. Res. Lett. 40, 3863–3867.
646 Connelly, D.P., Copley, J.T., Murton, B.J., Stansfield, K., Tyler, P.A., German, C.R., Van Dover,
647 C.L., Amon, D., Furlong, M., Grindlay, N., 2012. Hydrothermal vent fields and
648 chemosynthetic biota on the world's deepest seafloor spreading centre. Nat. Commun. 3,
649 620.
650 deMartin, B.J., Sohn, R.A., Canales, J.P., Humphris, S.E., 2007. Kinematics and geometry of
651 active detachment faulting beneath the Trans-Atlantic Geotraverse (TAG) hydrothermal
652 field on the Mid-Atlantic Ridge. Geology 35, 711–714. doi:10.1130/G23718A.1
653 Dick, H.J.B., Lin, J., Schouten, H., 2003. An ultraslow-spreading class of ocean ridge. Nature 426,
654 405. doi:10.1038/nature02128
655 Dunn, R. A., Lekić, V., Detrick, R. S., & Toomey, D. R. (2005). Three-dimensional seismic
656 structure of the Mid-Atlantic Ridge (35 N): Evidence for focused melt supply and lower
657 crustal dike injection. Journal of Geophysical Research: Solid Earth, 110(B9).
658 Escartín, J., Mével, C., Petersen, S., Bonnemains, D., Cannat, M., Andreani, M., Augustin, N.,
659 Bezos, A., Chavagnac, V., Choi, Y., Godard, M., Haaga, K., Hamelin, C., Ildefonse, B.,
660 Jamieson, J., John, B., Leleu, T., MacLeod, C.J., Massot-Campos, M., Nomikou, P., Olive,

J.A., Paquet, M., Rommevaux, C., Rothenbeck, M., Steinfuhrer, A., Tominaga, M., Triebe, L., Campos, R., Gracias, N., Garcia, R., 2017. Tectonic structure, evolution, and the nature of oceanic core complexes and their detachment fault zones (13°20′N and 13°30′N, Mid Atlantic Ridge). Geochem. Geophys. Geosystems 18, 1451–1482. doi:10.1002/2016GC006775

Escartín, J., Smith, D.K., Cann, J., Schouten, H., Langmuir, C.H., Escrig, S., 2008. Central role of detachment faults in accretion of slow-spreading oceanic lithosphere. Nature 455, 790.

Forsyth, D.W., 1992. Finite extension and low-angle normal faulting. Geology 20, 27–30.

Gerya, T. (2010) Dynamical instability produces transform faults at mid-ocean ridges. Science, 329, 1047-1050.

Gerya, T.V. (2013) Three-dimensional thermomechanical modeling of oceanic spreading initiation and evolution. Phys. Earth Planet. Interiors, 214, 35-52.

Gülcher, A.J.P., Beaussier, S.J., Gerya, T.V. (2019) On the formation of oceanic detachment faults and their influence on intra-oceanic subduction initiation: 3D thermomechanical modeling. Earth and Planetary Science Letters, 506, 195-208.

Harding, J.L., Van Avendonk, H.J.A., Hayman, N.W., Grevemeyer, I., Peirce, C., Dannowski, A., 2017. Magmatic-tectonic conditions for hydrothermal venting on an ultraslow-spread oceanic core complex. Geology 45, 839–842. doi:10.1130/G39045.1

Hayman, N.W., Grindlay, N.R., Perfit, M.R., Mann, P., Leroy, S., de Lépinay, B.M., 2011. Oceanic core complex development at the ultraslow spreading Mid-Cayman Spreading Center. Geochem. Geophys. Geosystems 12.

682 Hooft, E.E.E., Detrick, R.S., Toomey, D.R., Collins, J.A., and Lin, J., 2000, Crustal thickness and
683 upper mantle structure along three contrasting spreading segments of the Mid-Atlantic
684 Ridge: Journal of Geophysical Research, v. 105, no. B4, p. 8205–8226.
685 Howell, S.M., Ito, G., Behn, M.D., Martinez, F., Olive, J.-A., Escartín, J., 2016. Magmatic and
686 tectonic extension at the Chile Ridge: Evidence for mantle controls on ridge segmentation.
687 Geochem. Geophys. Geosystems 17, 2354–2373. doi:10.1002/2016GC006380
688 Ildefonse, B., Blackman, D.K., John, B.E., Ohara, Y., Miller, D.J., MacLeod, C.J., 2007. Oceanic
689 core complexes and crustal accretion at slow-spreading ridges. Geology 35, 623–626.
690 Ito, G., Behn, M.D., 2008. Magmatic and tectonic extension at mid-ocean ridges: 2. Origin of axial
691 morphology. Geochem. Geophys. Geosystems 9.
692 Kaus, B.J.P., A. A. Popov, T. S. Baumann, A. E. Pusok, A. Bauville, N. Fernandez, M. Collignon,
693 2016. Forward and Inverse Modelling of Lithospheric Deformation on Geological
694 Timescales. Presented at the NIC Symposium 2016.
695 Kuo, B.-Y., Forsyth, D.W., 1988. Gravity anomalies of the ridge-transform system in the South
696 Atlantic between 31 and 34.5 S: Upwelling centers and variations in crustal thickness. Mar.
697 Geophys. Res. 10, 205–232.
698 Lavier, L.L., Buck, W.R., Poliakov, A.N., 2000. Factors controlling normal fault offset in an ideal
699 brittle layer. J. Geophys. Res. Solid Earth 105, 23431–23442.
700 Liao, J., Gerya, T. (2015) From continental rifting to seafloor spreading: Insight from 3D thermo-
701 mechanical modeling. Gondwana Research, 28, 1329-1343.
702 Liu, Z., Buck, W.R., 2018. Magmatic controls on axial relief and faulting at mid-ocean ridges.
703 Earth and Planetary Science Letters 491, 226–237.

704 Macdonald, K.C., 1982. Mid-Ocean Ridges: Fine Scale Tectonic, Volcanic and Hydrothermal
705 Processes Within the Plate Boundary Zone. Annu. Rev. Earth Planet. Sci. 10, 155–190.
706 doi:10.1146/annurev.ea.10.050182.001103
707 MacLeod, C.J., Searle, R.C., Murton, B.J., Casey, J.F., Mallows, C., Unsworth, S.C., Achenbach,
708 K.L., Harris, M., 2009. Life cycle of oceanic core complexes. Earth Planet. Sci. Lett. 287,
709 333–344.
710 Olive, J.-A., Behn, M.D., Tucholke, B.E., 2010. The structure of oceanic core complexes
711 controlled by the depth distribution of magma emplacement. Nat. Geosci. 3, 491.
712 Olive, J.-A., Behn, M.D., 2014. Rapid rotation of normal faults due to flexural stresses: An
713 explanation for the global distribution of normal fault dips. J. Geophys. Res. Solid Earth
714 119, 2013JB010512. doi:10.1002/2013JB010512
715 Olive, J.-A., Behn, M.D., Ito, G., Buck, W.R., Escartín, J., Howell, S., 2015. Sensitivity of seafloor
716 bathymetry to climate-driven fluctuations in mid-ocean ridge magma supply. Science 350,
717 310–313, doi:10.1126/science.aad0715.
718 Parnell-Turner, R., Escartín, J., Olive, J.-A., Smith, D.K., Petersen, S., 2018. Genesis of corrugated
719 fault surfaces by strain localization recorded at oceanic detachments. Earth and Planetary
720 Science Letters 498, 116–128.
721 Parnell-Turner, R., R. A. Sohn, C. Peirce, T. J. Reston, C. J. MacLeod, R. C. Searle, N. M. Simão,
722 2017. Oceanic detachment faults generate compression in extension. Geology 45, 923–
723 926. doi:10.1130/G39232.1
724 Poliakov, A.N.B., Buck, W.R., 1998. Mechanics of Stretching Elastic-Plastic-Viscous Layers:
725 Applications to Slow-Spreading Mid-Ocean Ridges, in: Faulting and Magmatism at Mid-
726 Ocean Ridges. American Geophysical Union, pp. 305–323.

727 Püthe, C., Gerya, T.V. (2013) Dependence of mid-ocean ridge morphology on spreading rate in
728 numerical 3-D models. Gondwana Research, 25, 270-283.
729 Reston, T.J., Ranero, C.R., 2011. The 3-D geometry of detachment faulting at mid-ocean ridges.
730 Geochem. Geophys. Geosystems 12.
731 Saad, Y., 1993. A flexible inner-outer preconditioned GMRES algorithm. SIAM J. Sci. Comput.
732 14, 461–469.
733 Schouten, H., Smith, D.K., Cann, J.R., Escartín, J., 2010. Tectonic versus magmatic extension in
734 the presence of core complexes at slow-spreading ridges from a visualization of faulted
735 seafloor topography. Geology 38, 615–618.
736 Searle, R. C., MacLeod, C. J., Peirce, C., & Reston, T. J. (2019). The Mid-Atlantic Ridge near
737 13°20′N: High-resolution magnetic and bathymetry imaging. Geochemistry, Geophysics,
738 Geosystems, 20. doi:10.1029/2018GC007940
739 Sempéré, J.-C., Lin, J., Brown, H.S., Schouten, H., Purdy, G.M., 1993. Segmentation and
740 morphotectonic variations along a slow-spreading center: The Mid-Atlantic Ridge (24°00′
741 N– 30°40′ N). Mar. Geophys. Res. 15, 153–200. doi:10.1007/BF01204232
742 Shaw, P.R., 1992. Ridge segmentation, faulting and crustal thickness in the Atlantic Ocean. Nature
743 358, 491–493.
744 Shaw, W.J., Lin, J., 1996. Models of ocean ridge lithospheric deformation: Dependence on crustal
745 thickness, spreading rate, and segmentation. J. Geophys. Res. Solid Earth 101, 17977–
746 17993.
747 Smith, D.K., Cann, J.R., and Escartín, J., 2006, Widespread active detachment faulting and core
748 complex formation near 13°N on the Mid-Atlantic Ridge: Nature, v. 443, p. 440–444,
749 doi:10.1038/04950.

Smith, D.K., Escartín, J., Schouten, H., and Cann, J.R., 2008, Fault rotation and core complex formation: Significant processes in seafloor formation at slow-spreading mid-ocean ridges (Mid-Atlantic Ridge, 13 –15° N): Geochemistry, Geophysics, Geosystems, v. 9, no. 3, p. Q03003, doi:10.1029/2007GC001699.

ten Brink, U.S., Coleman, D.F., Dillon, W.P., 2002. The nature of the crust under Cayman Trough from gravity. Mar. Pet. Geol. 19, 971–987.

Thibaud, R., Gente, P., and Maia, M., 1998, A systematic analysis of the Mid-Atlantic Ridge morphology between 15°N and 40°N: Constraints of the thermal structure: Journal of Geophysical Research, v. 103, no. B10, p. 24233–24243.

Tian, X., Choi, E., 2017. Effects of axially variable diking rates on faulting at slow spreading mid-ocean ridges. Earth Planet. Sci. Lett. 458, 14–21.

Tucholke, B.E., Behn, M.D., Buck, W.R., Lin, J., 2008. Role of melt supply in oceanic detachment faulting and formation of megamullions. Geology 36, 455–458.

Tucholke, B.E., Lin, J., Kleinrock, M.C., 1998. Megamullions and mullion structure defining oceanic metamorphic core complexes on the Mid-Atlantic Ridge. Journal of Geophysical Research: Solid Earth 103, 9857–9866.

Van Avendonk, H.J., Davis, J.K., Harding, J.L., Lawver, L.A., 2017. Decrease in oceanic crustal thickness since the breakup of Pangaea. Nat. Geosci. 10, 58–61.

Acknowledgements: We wish to thank T. Gerya for his insightful review of this work, and the editor R. Bendick for her careful treatment of this manuscript. Further, we thank A. Popov for his role developing and supporting LaMEM, and E. Mittelstaedt and T. Morrow for their early contributions to this modeling effort. We owe our gratitude to the University of Hawai‘i for use of their High Performance Computing facility. This study was supported by NSF grants OCE-11-55098 and OCE-11-54238. Portions of this research were carried out at the Jet Propulsion Laboratory, California Institute of Technology, under contract with the National Aeronautics and Space Administration. Government sponsorship acknowledged.

Appendix A: Semi-Analytical Force Balance

The main concepts behind the force-balance-derived solutions for fault spacing are based on kinematic arguments, and supported by 2-D numerical models, that predict faults are active only on alternating sides of the ridge at a given time (Behn and Ito, 2008; Buck, 1993; Forsyth, 1992; Lavier et al., 2000). Near the onset of extension, slip on the active fault causes its strength to decrease (the above studies assumed a decrease in cohesion), and because it is the weakest point in the lithosphere, it is the only fault active at that distance y along the ridge axis. The active fault accommodates the full fraction of tectonic extension, $(1–M)$, on a single side of the ridge axis, while the magmatism in the neovolcanic zone accommodates the remaining fraction of extension, M. With time, plate separation accommodated by magma intrusion at the neovolcanic zone causes the fault to migrate away from the axis into thicker lithosphere, while continued slip on the fault causes the fault plane to rotate to a shallower dip and the attached lithosphere to bend. These changes lead to a steady increase in the force required to keep the fault active, and eventually the tensile stress becomes large enough that it is easier to break a new fault near the ridge axis than continue slip on the existing fault. At that point, the old fault stops slipping and a new fault takes up the tectonic fraction of extension, beginning the cycle anew.

The creation of the new fault occurs when

$$F_F + F_B \geq F_I, \tag{A1}$$

where F_I is the strength of the intact lithosphere near the ridge-axis (where the new fault forms), and the force required to keep the old fault active is the sum of the frictional strength of the fault, F_F, and the force required to bend the adjacent lithosphere, F_B (Lavier et al., 2000). The force required to initiate a new fault at the ridge axis is the depth-integrated yield strength of the

799 undamaged axial lithosphere (Behn and Ito, 2008; Forsyth, 1992), F_I, given by

800 $$F_I = \frac{\mu \rho g H_0^2 / 2 + H_0 C_0}{\mu \sin(\theta_0)^2 + \sin(\theta_0)\cos(\theta_0)}. \quad \text{(A2)}$$

801 Here μ is the coefficient of rock friction, ρ is the density, g is the acceleration due to gravity, H_0 is
802 the thickness of the brittle layer at the axis, C_0 is the initial cohesion of the undamaged lithosphere,
803 and θ_0 is the initial fault dip. The force required to overcome friction on the active fault plane is
804 similar to (A2), but includes the effects of changing lithosphere thickness H, fault dip θ, and
805 accumulated plastic strain ε_{aps},

806 $$F_F = \frac{\mu \rho g H^2 / 2 + H C(\varepsilon_{aps})}{\mu \sin(\theta)^2 + \sin(\theta)\cos(\theta)}. \quad \text{(A3)}$$

807 The force required to further bend the lithosphere with increasing slip is given by

808 $$F_B = A H^2 \left(1 - e^{-B \Delta h / H}\right), \quad \text{(A4)}$$

809 where A and B are empirically-derived elasto-plastic properties of the lithosphere and Δh is an
810 increment of fault heave, h (Lavier et al., 2000).

811 Changes in H, θ, and ε_{aps} are computed using finite differences and thus are described in terms
812 of increments of fault heave as follows. The thickness of the lithosphere is

813 $$H^h = H^{h-\Delta h} + \Delta x_{af} \frac{\partial H}{\partial x}, \quad \text{(A6)}$$

814 where $\partial H/\partial x$ is the lithosphere thickness gradient in the direction of spreading, x. Following Behn
815 and Ito (2008),

816 $$\frac{\partial H}{\partial x} = \begin{cases} H_0 / 20 \text{ km} & , \quad x \le 20 \text{ km} \\ 0 & , \quad x > 20 \text{ km} \end{cases}. \quad \text{(A7)}$$

817 Fault dip evolves with heave according to,

818 $$\theta^{h} = \theta^{h-\Delta h} - \frac{\partial \theta}{\partial h}\Delta h, \tag{A8}$$

819 where $\partial\theta/\partial h$ describes the rate of fault rotation with increasing heave (Behn and Ito, 2008). We
820 impose

821 $$\frac{\partial \theta}{\partial h} = \begin{cases} 5\ ^{\circ}/\mathrm{km} & , \quad \theta > 38^{\circ} \\ 0 & , \quad \theta \le 38^{\circ} \end{cases}. \tag{A9}$$

822 Finally, we can discretize equations Eqs. (A8) and (A9) to write accumulated plastic strain as a
823 function of incremental fault heave,

824 $$\varepsilon_{aps}^{h} = \left(\varepsilon_{aps}^{h-\Delta h} + \Delta h\sqrt{\left(\frac{1}{\Delta x}\right)^{2} + \left(\frac{\tan(\theta^{h})}{\Delta z}\right)^{2}}\left(\frac{\Delta t_{h}}{t}\right)\right)\left(1 + \frac{1}{\varepsilon}\right)^{-1}, \tag{A13}$$

825 Where Δx and Δz are width and height of the localized model shear band, respectively, used to
826 calculate incremental strain in the dip-direction.

827 The off-axis distance of the active fault HCO (termination), x_T, increases by Δx_T for an increase
828 in fault heave of Δh according to

829 $$x_T^{h} = x_T^{h-\Delta h} + \Delta x_T, \quad \Delta x_T = \Delta h\left(\frac{2M-1}{2}\right). \tag{A5}$$

830 The increment of heave is related to an increment in time through rate at which the active fault
831 HCO migrates off-axis, u_{TA}, which depends on the half spreading rate $u_{1/2}$ and M,

832 $$u_{TA} = u_{1/2}\left(2M - 1\right). \tag{A10}$$

833 The rate at which the fault accumulates heave is the difference between the migration rates at of

the fault cutoffs,

$$u_{½} - u_{TA} = 2u_{½}\left(1 - M\right). \tag{A11}$$

This is then used to find the time increment,

$$\Delta t_h = \frac{\Delta h}{2u_{½}\left(1 - M\right)}. \tag{A12}$$

This is the time increment used with backward finite differences to solve for the evolution of H (A6, A7), fault dip (A8, A9), and accumulated plastic strain (A13). These quantities then are used to update F_F (A3) and F_B (A4). The time at which the force equation (A1) is met determines x_c. The final locations of each of the fault boundaries are then given by Equations (2) and (3) in the main text.

Appendix B: Mathematical and Numerical Method

The configuration and boundary conditions of the 3-D numerical model is shown in **Figure 3** and is described in the text. A list of symbol descriptions, units and values is provided in Table B1. The above system is modelled mathematically by solving the equations for conservation of mass and conservation of momentum for a viscous continuum with zero Reynolds number,

$$\frac{\partial v_i}{\partial x_i} = \begin{cases} 0 & , \text{ outside of MIZ} \\ \dfrac{2Mu_{1/2}}{w_{\mathrm{MIZ}}} & , \text{ inside of MIZ} \end{cases}, \tag{B1}$$

$$\frac{\partial \sigma'_{ij}}{\partial x_j} - \frac{\partial P}{\partial x_i} = -\rho g_i . \tag{B2}$$

Here, repeated indices in a term imply summation over the three index values, denoting the three Cartesian directions. In the continuity equation (B1), v_i and x_i are respectively the Cartesian components of velocity and position, w_{MIZ} is the width of the magma injection zone (here, one element wide), and $u_{1/2}$ is the half-spreading-rate. In the momentum equation (B2), σ'_{ij}, P, ρ, and g_i are respectively the deviatoric stresses, pressure, density, and acceleration due to gravity.

Simulating the MIZ is done by imposing a non-zero source term to the continuity equation that results in the desired change in velocity across the MIZ. This is preferable to specifying the absolute velocity on either side of the injection zone because the imposed divergence allows the associated velocities in x and z to respond dynamically to lithospheric stresses, and allows faulting to occur on one side or both sides of the ridge axis (illustrated in Figure B1).

This system of equations is closed with a constitutive law that relates deviatoric stresses to strain rates $\dot{\varepsilon}_{ij}$. The constitutive relation captures ductile (viscous) deformation in the

asthenosphere and warmer parts of the lithosphere, the elastic flexure of the lithosphere, and the brittle (plastic) failure of lithosphere faults. Ductile deformation is controlled by a creep viscosity, η_v and is an Arrhenius function of temperature with an activation energy of 200 kJ/mol, and elasticity is introduced by assuming the material acts as a Maxwell solid.

Finally, brittle failure is simulated by limiting the effective viscosity such that the second invariant of deviatoric stress, τ'_{II}, never exceeds the yield stress, σ_Y,

$$\eta_{vep} = \begin{cases} \eta_{ve} & , \tau'_{II} < \tau_Y \\ \dfrac{\tau_Y}{2\dot{\varepsilon}_{II}} & , \tau'_{II} \geq \tau_Y \end{cases} . \quad \text{(B3)}$$

The yield stress is determined by enforcing the Drucker-Prager form of the Mohr-Coulomb yield criterion,

$$\tau_Y = P \sin(\phi) + C \cos(\phi), \quad \text{(B4)}$$

where ϕ is the friction angle and C is the cohesion.

The deformation in regions limited by σ_Y is referred to as "plastic" strain, and these deformation regions tend to localize in bands that resemble fault zones. This plastic deformation is tracked through time and used to calculate an accumulated plastic strain, ε_{aps}. We impose a cohesion law such that C decreases linearly with ε_{aps} to simulate damage-induced weakening of rock material (Poliakov and Buck, 1998),

$$C = \begin{cases} 1 - \left(\dfrac{\varepsilon_{aps} - \varepsilon_{crit,1}}{\varepsilon_{crit,2} - \varepsilon_{crit,1}} \right) & , \varepsilon_{crit,1} \leq \varepsilon_{aps} \leq \varepsilon_{crit,2} \\ 0 & , \varepsilon_{aps} \geq \varepsilon_{crit,2} \end{cases} , \quad \text{(B5)}$$

where C_0 is the initial cohesion, $\varepsilon_{crit,1}$ is the critical strain required for the onset of cohesion loss,

and $\varepsilon_{crit,2}$ is the critical strain required for full cohesion loss. In addition to this weakening mechanism, we simulate "healing" of the damaged rock by decreasing the accumulated plastic strain between successive time steps Δt (Poliakov and Buck, 1998),

$$e^{t}_{aps} = e^{t-\Delta t}_{aps} \left(\frac{\Delta t}{\tau} + 1 \right)^{-1} . \quad \text{(B6)}$$

The rate of healing is controlled by the timescale, τ. Thus, plastic shear deformation tends to localize into bands (fault zones) when tectonic plastic strain growth outpaces the time-healing decay, and accumulated strain builds to the critical value.

Numerical aspects

We apply the Flexible-GMRES (Saad, 1993) Krylov method to solve Eqs. B1 and B2, preconditioned with a coupled geometric Galerkin multigrid preconditioner that smoothens for pressure and velocity simultaneously, with 1/viscosity at the pressure block in the preconditioner (Cai et al., 2014).

Support for all parallel linear algebra, in the form of matrices, vectors, preconditioners, Krylov methods and nonlinear solvers is provided by PETSc (Balay et al., 2017, 1997). Parallelism is achieved by spatially decomposing the structured finite difference grid with several DMDA objects as provided by PETSc.

The simulations were performed using the University of Hawai‘i High Performance Computing cluster, which has 178 standard compute nodes consisting of two Intel Xeon E5-2680v2 "Ivy Bridge" 10-core, 2.8GHz processors. Each model was run on 64-256 cores distributed over 4-13 nodes. The models required approximately 900 time steps, summing to approximately~1 day of computation time for a mesh resolution of 256 × 64 × 128 finite difference elements, and

902 14 days of computation time for a mesh of 256 × 256 × 128.

903 The multigrid preconditioner was configured with five levels. For the largest models, the
904 number of elements from the coarsest to the finest level were: 16×16×8, 32×32×16, 64×64×32,
905 128×128×64, 256×256×128. The coarse grid solver was a parallel direct solver (superlu_dist). The
906 non-linear SNES solver uses Newton iterations, with the convergence criteria being either a
907 relative tolerance (rtol) of 10^{-3} or absolute tolerance (atol) of 10^{-2} and an Eisenstatt-Walker
908 algorithm, combined with line search (cp). The inner linear KSP solver is terminated when relative
909 tolerance 10^{-4}, an absolute tolerance of 10^{-3}, or 15 iterations are reached. Two smoothening steps
910 are used at every level of the multigrid algorithm using Chebyshev/SOR iterations.

911 LaMEM (Kaus et al., 2016) is an open source code released under the GNU General Public
912 License v.3 and may be accessed at https://bitbucket.org/bkaus/LaMEM. LaMEM leverages
913 functionality from PETSc, which can be freely downloaded at http://www.mcs.anl.gov/petsc. For
914 this paper we used the branch /dike_injection and commit version 53a3f43. Input files are available
915 upon request from the corresponding author.

916 **Table B1:** Descriptions, values, and units for model parameters.

Symbol	Description	Value	Units
v_i	Velocity field		
x_i	Cartesian position		
M	Fraction of magmatic extension	0.5–0.9	-
$u_{1/2}$	Ridge half-spreading rate	12.5	km/Myr
w_{MIZ}	Magma injection zone width	317	m
σ'_{ij}	Deviatoric stress		
P	Pressure		
ρ	Density	1,000–3,300	kg/m^3
g_i	Gravitational acceleration	9.81	m/s^2
$\dot{\varepsilon}_{ij}$	Strain rate		
η_v	Lithosphere creep viscosity	1×10^{18}–1×10^{24}	Pa s
G	Elastic shear modulus	40	GPa
Δt	Computational visco-elastic timestep	< 3.9	kyr
η_{ve}	Visco-elastic viscosity	< 1×10^{24}	Pa s
ζ	Visco-elastic ratio		
σ_Y	Yield stress		
C_0	Initial cohesion	30	MPa
	Friction angle	30	degrees
ε_{aps}	Accumulated plastic strain		
$\varepsilon_{crit,1}$	Critical ε_{aps} for onset of cohesion loss	0.02	-
$\varepsilon_{crit,2}$	Critical ε_{aps} for full cohesion loss	0.1	-
τ	Plastic healing timescale	20	kyr
η_{vep}	Full visco-elasto-plastic viscosity	< 1×10^{24}	Pa s
H_0	Axial lithosphere thickness	4, 6	km
H	Lithosphere thickness	4–8, 6–12	km

917

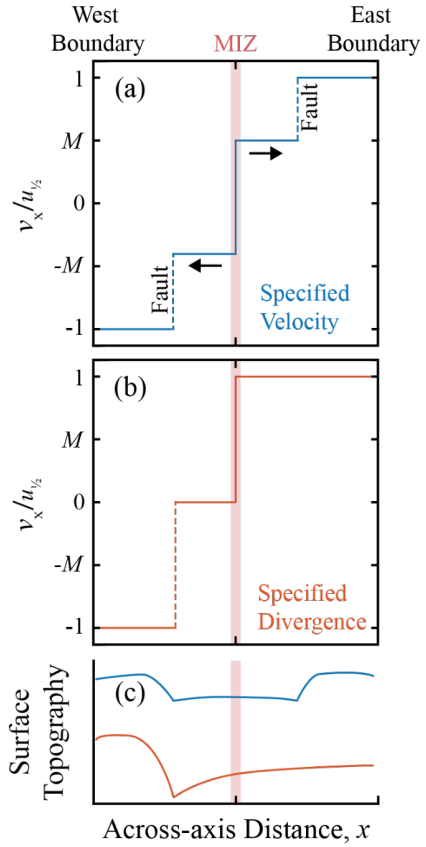

Figure B1: Schematic of lithosphere velocities, v_x, for a magma injection zone (MIZ) imposed through (a) specified velocity on either side of the MIZ and (b) specified divergence across the MIZ. (c) Corresponding cartoons of surface topography for velocity (blue) and divergence (orange) specification. Imposing velocities on the sides of the MIZ would force faulting to occur on both sides of the ridge axis, whereas imposing a divergence in the MIZ allows faulting to respond dynamically, sometimes occurring on one side of the ridge axis and other times occurring on both sides.